chemosensors

MDPI

Article

An Activatable Fluorescence/Photoacoustic Bimodal Probe for the Detection of Drug-Induced Liver Senescence

Ying-Hong Yan, Jun-Liang Zhou, Li-Li Ren, Ping-Zhao Liang, Wen Zhang, Tian-Bing Ren, Lin Yuan, Xia Yin * and Xiao-Bing Zhang *

College of Chemistry and Chemical Engineering, Hunan University, Changsha 410082, China; yanyinghong0728@hnu.edu.cn (Y.-H.Y.); zjl1046@hnu.edu.cn (J.-L.Z.); llren@hnu.edu.cn (L.-L.R.); lpingzhao98@hnu.edu.cn (P.-Z.L.); wenzhang0133@hnu.edu.cn (W.Z.); rentianbing@hnu.edu.cn (T.-B.R.); lyuan@hnu.edu.cn (L.Y.)

* Correspondence: yinxia@hnu.edu.cn (X.Y.); xbzhang@hnu.edu.cn (X.-B.Z.)

Abstract: Senescence is an intricate physiological progression that can be instigated by a multiplicity of factors. Aberrant cellular senescence is capable of precipitating a substantial array of diseases. During chemotherapy, drugs typically tend to gradually accumulate in the liver, thereby inducing liver senescence and leading to a successive deterioration in its physiological function. β-galactosidase (β-gal), serving as a significant index in the exploration of senescence, has attracted considerable attention. In this study, a fluorescence/photoacoustic (FL/PA) biomodal probe (Gal-QCS) was developed based on a hemicyanine fluorophore for the imaging of β-gal in the process of drug-induced liver senescence. Gal-QCS demonstrates rapid responsiveness, high sensitivity, and remarkable selectivity in detecting β-gal in aqueous solutions. After incubation with β-gal, the fluorescence signal at 810 nm significantly increases, and concurrently, the photoacoustic signal at 775 nm also exhibits a substantial increment. Upon the induction of cell senescence with camptothecin, Gal-QCS can expeditiously and selectively image senescent cells. Moreover, after administering this probe to mice with liver senescence, the FL/PA signals in the livers of senescent mice were enhanced by 10.53-fold and 1.43-fold, respectively. This work robustly substantiates the potential and application prospects of Gal-QCS in detecting drug-induced liver senescence, with β-gal serving as a biomarker.

Keywords: β-galactosidase; fluorescence; photoacoustic; probe; senescence; imaging

Received: 20 December 2024
Revised: 10 February 2025
Accepted: 14 February 2025
Published: 17 February 2025

Citation: Yan, Y.-H.; Zhou, J.-L.; Ren, L.-L.; Liang, P.-Z.; Zhang, W.; Ren, T.-B.; Yuan, L.; Yin, X.; Zhang, X.-B. An Activatable Fluorescence/Photoacoustic Bimodal Probe for the Detection of Drug-Induced Liver Senescence. *Chemosensors* **2025**, *13*, 74. https://doi.org/10.3390/chemosensors13020074

1. Introduction

The dynamic balance between cellular senescence and proliferation is the foundation for maintaining the normal life activities of the organism [1–4]. However, abnormal cellular senescence is a major risk factor associated with many pathological conditions [5–7]. Chemotherapy, as one of the important strategies for cancer treatment, has been widely applied in clinical settings [8,9]. However, it has been reported that the accumulation of chemotherapy drugs within normal organs (particularly the liver) during the metabolic process can aggravate the senescence and injury of relevant organs [10,11]. This is because one of the mechanisms of chemotherapeutic drugs is to induce DNA damage within cells, thereby inhibiting cell proliferation. Such DNA damage will activate the intracellular DNA damage repair mechanism. Nevertheless, if the damage is too severe and renders the cell unable to complete effective repair, it will lead to cell cycle arrest and further accelerate tissue senescence [12,13].

Drug-induced liver senescence can seriously affect the metabolic and detoxification functions of the liver and accelerate the senescence process of the body. Therefore, early diagnosis of drug-induced liver senescence is vital for subsequent treatment. Currently, a variety of biomarkers have been reported to be involved in the cellular senescence process, such as cyclin-dependent kinase inhibitors (P21 and P53), anti-apoptotic proteins, and β-galactosidase (β-gal) [14,15]. Among them, β-gal, as an important biomarker that is over-expressed in senescent cells, has attracted extensive attention in many studies [16–19].

Near-infrared fluorescence (NIRF) imaging technology has received increasing attention in the field of in vivo imaging due to its remarkable advantages such as high sensitivity, low background fluorescence interference, and non-invasive visualization. Fluorescence imaging technology based on small organic molecule probes has become a powerful tool for specific and selective imaging of enzyme activity in complex biological systems. Currently, numerous fluorescence probes for detecting aging have been developed [7,20–23]. Although fluorescence probes with wavelengths in the NIR region have a better imaging signal-to-noise ratio and less light damage, they are still limited by the in vivo penetration depth (<1 mm). Due to its limited penetration depth, it is restricted in clinical applications. In contrast, photoacoustic (PA) imaging can overcome light scattering by detecting the acoustic signals from the thermal expansion of excited contrast agents. It combines high-contrast optical imaging with the high spatial resolution of ultrasound, breaking through the depth limitation of pure optical imaging and enabling imaging of deep tissue [24–27]. However, the relatively low sensitivity of photoacoustic imaging poses challenges in obtaining clear images of some biological tissues with low absorption and low scattering. Due to the complementary characteristics of NIRF and PA, the combined use of NIRF and PA is considered a promising approach. It can not only achieve functional imaging with high sensitivity and depth but also provide high-resolution structural information for in vivo research [28–30]. In recent years, there have been some reports on FL/PA dual-mode imaging probes for detecting β-gal [31]. However, the vast majority of these studies concentrate on imaging-based evaluations of tumor treatment outcomes and have yet to extend this technology to the detection of organ senescence. We aim to develop an FL/PA dual mode probe that can precisely image the drug-induced liver senescence process. This development holds great significance for prognosing the liver's health status following drug treatment.

Herein, we have designed and synthesized an FL/PA dual-mode probe Gal-QCS, enabling the visualization detection of drug-induced liver senescence at the in vivo level. As shown in Figure 1, the probe Gal-QCS adopts hemicyanine dye Bn-QCS as its framework, with glycosidic bonds connected to the dye via a self-immolative linker. The hydroxyl group of hemicyanine is locked, thereby inhibiting the intramolecular charge transfer (ICT). The glycosidic bond is selectively cleaved only in the presence of β-gal, exposing the hydroxyl group and restoring the FL/PA signal. The probe Gal-QCS has almost no fluorescence and photoacoustic signals in its initial state. After being incubated with β-gal, the fluorescence signal at 810 nm and the photoacoustic signal at 775 nm gradually recover. Subsequently, we verified at the cellular level that Gal-QCS can effectively image drug-induced senescent cells. Finally, through the real-time changes in FL/PA signals, we visually demonstrated that chemotherapy drugs can induce liver senescence in mice. As expected, the probe Gal-QCS demonstrated outstanding performance in the detection of β-gal, characterized by extremely high selectivity, sensitivity, and a rapid reaction rate. Of particular importance, this probe has been successfully applied in a drug-induced liver senescence mouse model, enabling precise detection of β-gal in vivo. It is firmly believed that the Gal-QCS probe can serve as an effective tool for monitoring the dynamic changes in organ senescence during the progression of in vivo pathological processes.

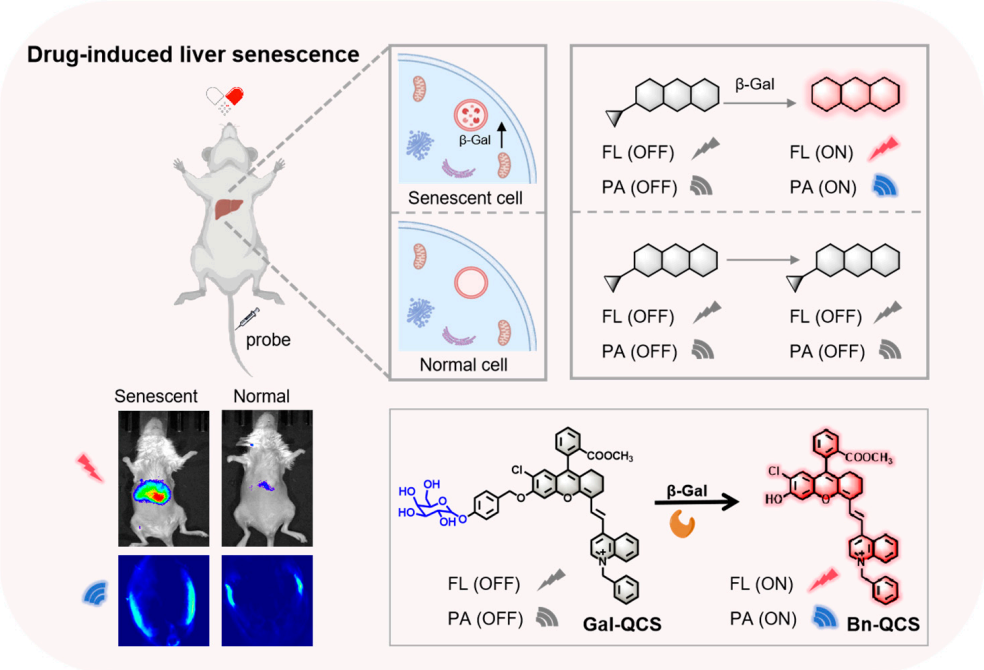

Figure 1. Schematic illustration of Gal-QCS activated by β-gal and its application in detecting senescent cells.

2. Materials and Methods

Materials and instruments. Unless otherwise stated, all reagents were purchased from commercial suppliers and used without further purification. Solvents used were purified by standard methods prior to use. Twice-distilled water was used throughout all experiments. The compounds purchased for the experiment are listed in Table S1. All enzymes and analytes mentioned were purchased from Sigma-Aldrich. TLC analysis was performed on silica gel plates and column chromatography was conducted over a silica gel (mesh 200–300), both of which were obtained from Qingdao Ocean Chemicals. Mass spectra were performed using Matrix Assisted Laser Desorption Ionization Time of Flight Mass Spectrometry (ultrafle Xtreme). NMR spectra were recorded on a Bruker-400 spectrometer, using TMS as an internal standard. UV-Visible absorption spectra were acquired via a Shimadzu UV-2600 UV-VIS-NIR spectrophotometer. Photoluminescent spectra were recorded at room temperature with a HITACHI F7000 fluorescence spectrophotometer (1 cm standard quartz cell). The cell fluorescence images were acquired with a Nikon A1plus confocal microscope (Nikon, Japan); The in vivo (living mice) imaging was carried out using an IVIS Lumina XR (IS1241N6071) in vivo imaging system; Photoacoustic images of mice were obtained from MSOT in Vision 256-TF (iThera Medical GmbH, Munich, Germany). The pH measurements were carried out on a Mettler-Toledo Delta 320 pH meter. H&E staining images were acquired from Wuhan Servicebio Technology.

Synthesis of probe Gal-QCS. Gal-QCS was synthesized according to Scheme 1. The details of the synthesis steps are listed in the Supporting Information [32–34]. The NMR characterization of the synthesized compound can be seen in Figures S12–S14.

Preparation of the Cell Imaging Experiment. Hela cells are cultured in high-glucose Dulbecco's Modified Eagle Medium (DMEM, Hyclone) supplemented with 10% of fetal bovine serum (FBS, from BI) and 1% of antibiotics (100 U/mL penicillin and 100 μg/mL streptomycin, from Hyclone) at 37 °C with 5% carbon dioxide. 4T1 cells are cultured in Roswell Park Memorial Institute 1640 medium (1640, Hyclone) supplemented with 10% of fetal bovine serum (FBS, from BI) and 1% of antibiotics (100 U/mL penicillin and 100 μg/mL streptomycin, from Hyclone) under the same conditions of 37 °C and

5% carbon dioxide. When the cell confluence reaches 80%, the cells are carefully harvested and passaged to maintain their exponential growth state. After completing the cell passage procedure, we carefully inoculated the cells into confocal dishes. When the cell density reaches the range of 70 to 80%, subsequent imaging studies can be carried out. The confocal dish was placed in an incubator. After the cells were washed several times with Dulbecco's Phosphate-Buffered Saline (DPBS), they were used for confocal imaging. The cultured Hela cells were incubated with the drug camptothecin (CPT) for 36 h to induce cell senescence, and then the probe Gal-QCS was added and incubated for 30 min. The cell senescence was imaged with a confocal microscope. The excitation wavelength is 640 nm, and the emission range is 663–738 nm.

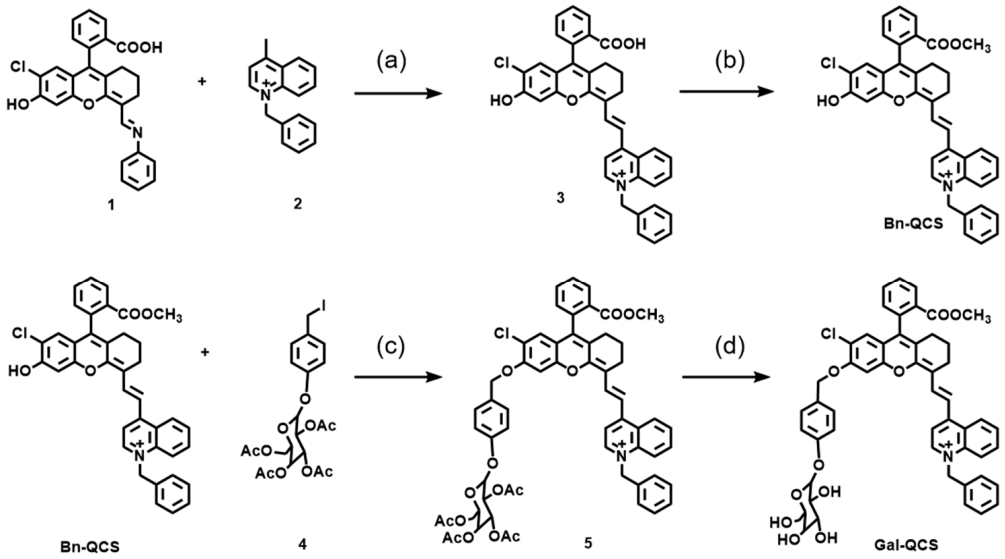

Scheme 1. Synthetic route for the probe Gal-QCS. (**a**) pyridine, 90 °C, 3 h. (**b**) MeOH, H_2SO_4, 90 °C, 8 h. (**c**) MeCN, DIPEA, 85 °C, 6 h. (**d**) MeOH, K_2CO_3, r.t.,1 h.

Cell Cytotoxicity. The cytotoxicity of Gal-QCS on 4T1 and Hela cells was evaluated by MTT (Methylthiazolyldiphenyl-tetrazolium bromide) assay. The 4T1 cells and Hela cells were seeded in a 96-well plate for 24 h. Then, the cells were incubated with Gal-QCS at various concentrations (0–30 μM) for another 24 h. After that, the solution in each well was replaced with 200 μL of MTT (0.5 mg/mL). After incubation for 5 h, the supernatant was aspirated and 200 μL of DMSO was added. The absorbance of the solution at 490 nm was recorded using a microplate reader. The biocompatibility of the probe was verified by calculating the cell survival rate.

In Vitro Imaging. All photoacoustic images were analyzed and collected at various time points by an In Vision 256-TF imaging system. The testing system utilized a 30% EtOH/PBS buffer. The concentration of the probe Gal-QCS was set at 5 μM, and the concentration of β-Gal was 2 U/mL. The test samples were divided into two groups: the Gal-QCS group and the Gal-QCS + β-gal group. The test solutions were placed in 300 μL centrifuge tubes for imaging. During imaging, the centrifuge tubes were placed in a 37 °C water bath. Data were collected at a 0.3 mm step along the selected area of the centrifuge tube. When measuring the probe's response, the centrifuge tubes were pre-incubated at 37 °C for 30 min to ensure a saturated response. Subsequently, they were placed in the instrument to collect photoacoustic data within the wavelength range of 720 nm to 900 nm. When testing the kinetics, the imaging wavelength was 775 nm. The centrifuge tubes were directly placed into the photoacoustic instrument, and then data were collected every 0.5 min to observe the changes in the photoacoustic signals.

In Vivo Imaging. All animal experiments were carried out in strict accordance with relevant laws and regulations, and were officially approved by the Institutional Animal Care and Use Committee of Hunan University (Permit No.: SYXK 2018-0006). The female BALB/c mice used in the experiments, aged 5–6 weeks, were purchased from Hunan Anshengmei Pharmaceutical Research Co., Ltd. (Changsha, China). We selected female BALB/c mice within this age range with the aim of establishing a drug-induced senescence animal model suitable for in vivo imaging studies. After the mice were purchased, they were first raised for 1 week. Subsequently, the experimental drug camptothecin (CPT) was dissolved in a mixed system composed of 10% ethanol and phosphate buffered saline (PBS), and administered to the mice by gavage in a dose of 6 mg/kg. The dosing frequency was set at once every 2 days. After a complete 8-day dosing cycle, a senescent mouse model was successfully established. As a control, the normal mouse group received intragastric administration of PBS. Before the imaging detection, all mice were required to fast for 12 h. After that, 100 μL of Gal-QCS solution (a 100 μmol/L PBS solution containing 20% ethanol) was injected into the mice via the tail vein, and then the imaging operation was carried out immediately. The fluorescence imaging was carried out using an IVIS Lumina XR (IS1241N6071) in vivo imaging system, the excitation wavelength for this imaging was set at 710 nm, and the collection wavelength was 820 nm–880 nm. Photoacoustic images of mice were obtained from MSOT in Vision 256-TF (iThera Medical GmbH, Munich, Germany). The collection wavelength for photoacoustic imaging was 775 nm.

3. Results

3.1. Rational Design of Gal-QCS

In previous studies, our group developed a series of hemicyanine fluorophores using a hybridization strategy. These dyes have several ideal properties, including easily modifiable structures, low autofluorescence interference, and excellent stability. They have already been successfully utilized in deep-tissue fluorescence and photoacoustic imaging. However, the absorption and emission wavelengths of these dyes are relatively short. Moreover, our group previously reported that substituting the indole moieties of hemicyanine dye with a quinoline group can prolong the wavelength of classic hemisalicylic acid dyes and adjust the FL/PA signal output, which is conducive to the improvement of the FL/PA bimodal scaffold [33]. From another perspective, the potential aggregation issue of this dye can be effectively addressed by introducing larger rotational groups with stronger steric hindrance effects. Therefore, we introduced methyl and benzyl substituents to the quinoline group and conducted spectral tests in 30% EtOH/PBS. The results indicate that the dye with a methyl substitution (QCS) shows a strong aggregation phenomenon, whereas the benzyl group (Bn-QCS) can alleviate this aggregation issue (Figure S1). Based on this, we used benzylquinoline modified hemicyanine dye (Bn-QCS, Φ_F = 0.22%) as a scaffold and connected pyran galactoside as the recognition unit of β-gal to successfully develop a FL/PA bimodal probe (Gal-QCS) (Figure 2). To date, a great number of probes based on the hemicyanine skeleton have been reported, and their response processes rely heavily on the intramolecular charge transfer (ICT) effect [31]. Therefore, we hypothesize that protecting the hydroxyl group of Bn-QCS would disrupt the ICT effect, thereby quenching the FL/PA signals. In the presence of β-gal, the glycosidic bond undergoes hydrolysis, triggering an intramolecular self-elimination reaction that releases the hydroxyl group of Bn-QCS. This process restores the ICT effect, thereby simultaneously activating the FL/PA signals.

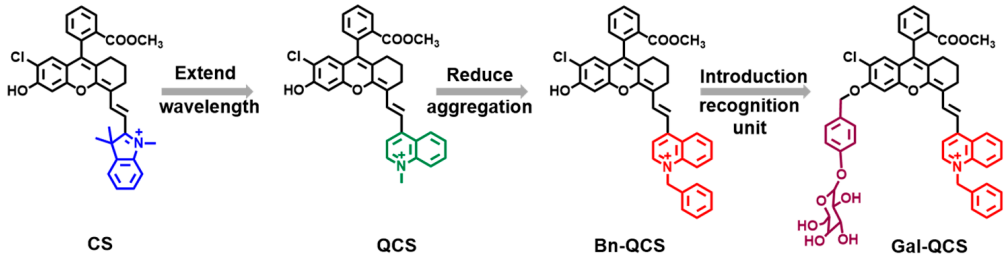

Figure 2. Design strategy of Gal-QCS.

3.2. Spectroscopic Response of Gal-QCS to β-Gal

As shown in Figure 3a, the cage effect of the glycoside group restricts the ICT within the fluorophore, resulting in an initial absorption peak of Gal-QCS at 620 nm. After incubating with the β-gal (2 U/mL) solution (EtOH/PBS = 3:7, *v*/*v*, pH 7.4) at 37 °C for 30 min, the absorption peak of Gal-QCS at 620 nm disappeared, and a new absorption peak appeared at 775 nm. The color of the solution obviously changed from blue to green. Notably, the color change and bathochromic shift are consistent with the optical properties of the fluorophore Gal-QCS. Furthermore, the fluorescence intensity at 810 nm and the photoacoustic intensity at 775 nm of Gal-QCS were initially very weak. After incubation with β-gal, the fluorescence intensity at 810 nm and the photoacoustic intensity at 775 nm were enhanced by 10.6-fold and 10.5-fold, respectively (Figure 3b,c), demonstrating the excellent FL/PA bimodal response of Gal-QCS to β-gal. Meanwhile, to ensure consistency between in cell experiments and in vivo experiments, we also used a 640 nm laser for excitation and collected spectra in the range of 660 nm to 900 nm (Figure S2). In addition, to further understand the enzyme kinetics of the probe, the change in the fluorescence intensity of Gal-QCS over time was measured when it was incubated with β-gal (2 U/mL). As shown in Figure 3d, the fluorescence increased rapidly within 5 min and reached a plateau at 10 min, indicating a rapid response of the probe Gal-QCS to β-gal. Meanwhile, we also tested the time-dependent photoacoustic dynamics; as depicted in Figure S3, the photoacoustic intensity increased rapidly within five minutes, and this is consistent with the fluorescence enhancement trend. Moreover, the Michaelis–Menten equation was constructed. The kinetic parameter Michaelis constant (Km) was calculated to be 12.03 μmol/L, and the results demonstrated that Gal-QCS has a good affinity for β-gal. More importantly, Gal-QCS, which has an excellent affinity for β-gal, may be an ideal choice for the rapid detection and high-fidelity imaging of the enzyme in biological scenarios. According to the spectral results, we speculated that during the reaction with β-gal, the original structure of Gal-QCS changed. This transformation is attributed to the specific hydrolysis of the glycosidic bond by β-gal, which exposed the hydroxyl group of Bn-QCS, inducing ICT and activating FL/PA signals.

To further verify the sensing mechanism of the probe Gal-QCS for β-gal, we used MALDI-TOF (matrix-assisted laser desorption/ionization time-of-flight) mass spectrometry to detect the reaction between the probe Gal-QCS and β-gal. We found that when co-incubating Gal-QCS and β-gal, the signal at m/z = 880.254 is decreased and the signal at m/z = 613.217 is enhanced (Figures S4–S6), which is highly consistent with the theoretical simulation of the proposed sensing process. Next, we explored the detection sensitivity of the probe Gal-QCS to β-gal by detecting the response of Gal-QCS to various concentrations of β-gal. As shown in Figure 4a, within the range of 0–1.6 U/mL, the absorbance of Gal-QCS at 775 nm gradually increased with rising β-gal concentrations. At the same time, its fluorescence intensity at 810 nm also increased (Figure 4b). When the concentration of β-gal is in the range of 0–0.2 U/mL, the fluorescence intensity showed a linear increase (Figures 4c and S7). The limit of detection (LOD) for Gal-QCS in fluorescence detection

is 4.3 mU/mL. In addition, we also recorded the photoacoustic intensity of Gal-QCS at 775 nm incubated with different concentrations of β-gal (0–1.2 U/mL) (Figure 4d). In the presence of β-gal, the photoacoustic intensity at 775 nm is significantly enhanced and exhibited a linear relationship within the range of 0–0.1 U/mL (Figures 4e and S8). The limit of detection (LOD) for Gal-QCS in photoacoustic detection is 6.7 mU/mL. These results are consistent with the fluorescence detection findings. In conclusion, Gal-QCS can be used for sensitive detection of β-gal in a dual mode of FL/PA imaging.

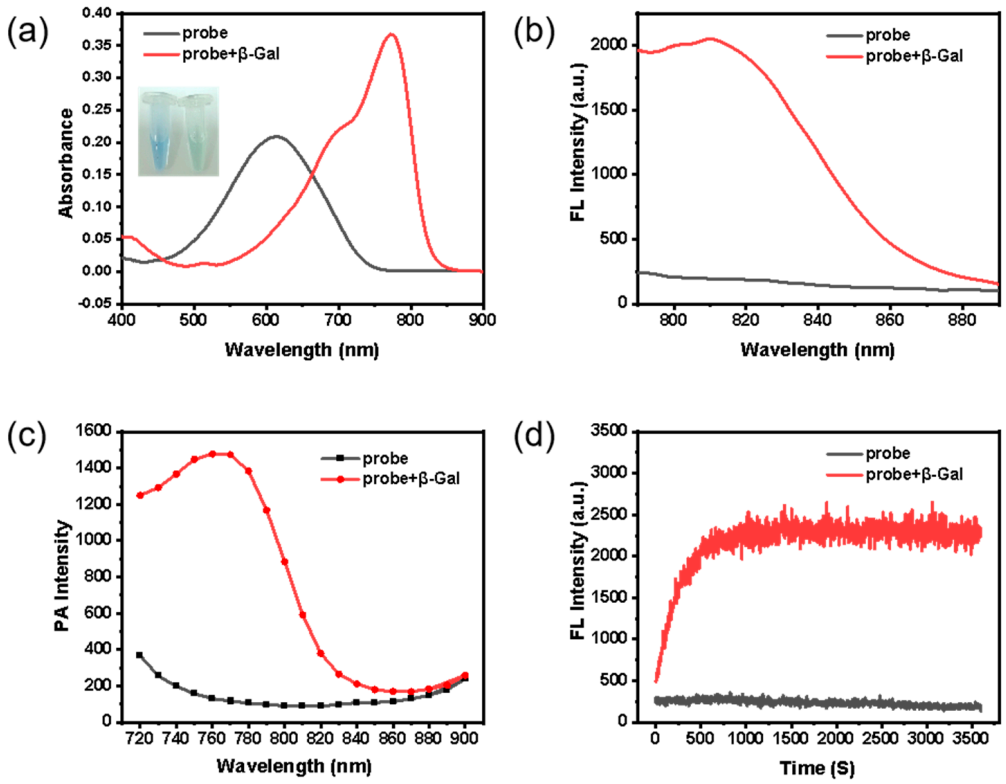

Figure 3. Optical response of Gal-QCS (5 μM) to β-gal. (**a**) Absorption and (**b**) fluorescence spectral changes in Gal-QCS in the presence of β-gal (2 U/mL). Ex = 760 nm. (**c**) photoacoustic spectra of 5 μM Gal-QCS with 2 U/mL β-gal. (**d**) Time-dependent fluorescence response of Gal-QCS (5 μM) to β-gal (2 U/mL).

We further studied the selectivity and pH dependence of Gal-QCS for β-gal to verify the detection ability of Gal-QCS for β-gal in a physiological environment. As shown in Figure 4f, after incubating Gal-QCS (5 μM) with potentially interfering biological substances (including cations, reducing anions, reactive oxygen species, amino acids, and enzymes) for 30 min, only the Gal-QCS solution treated with β-gal exhibited a 45-fold increase in the absorption signal at 775 nm. After incubation with other interfering species, the absorption signal at 775 nm hardly showed a significant increase, indicating the high selectivity of Gal-QCS for β-gal. In addition, we detected the influence of pH on the response of Gal-QCS. As shown in Figure S9, the fluorescence of Gal-QCS remained relatively stable within the pH range of 5.0–8.0 in the absence of β-gal. In contrast, in the presence of β-gal, the fluorescence intensity of Gal-QCS increased within the same pH range; this is also consistent with the good catalytic activity of β-gal within this range. These results confirm the pH stability of Gal-QCS. In conclusion, its excellent selectivity and pH stability prove the feasibility of Gal-QCS for detecting β-gal in a physiological environment.

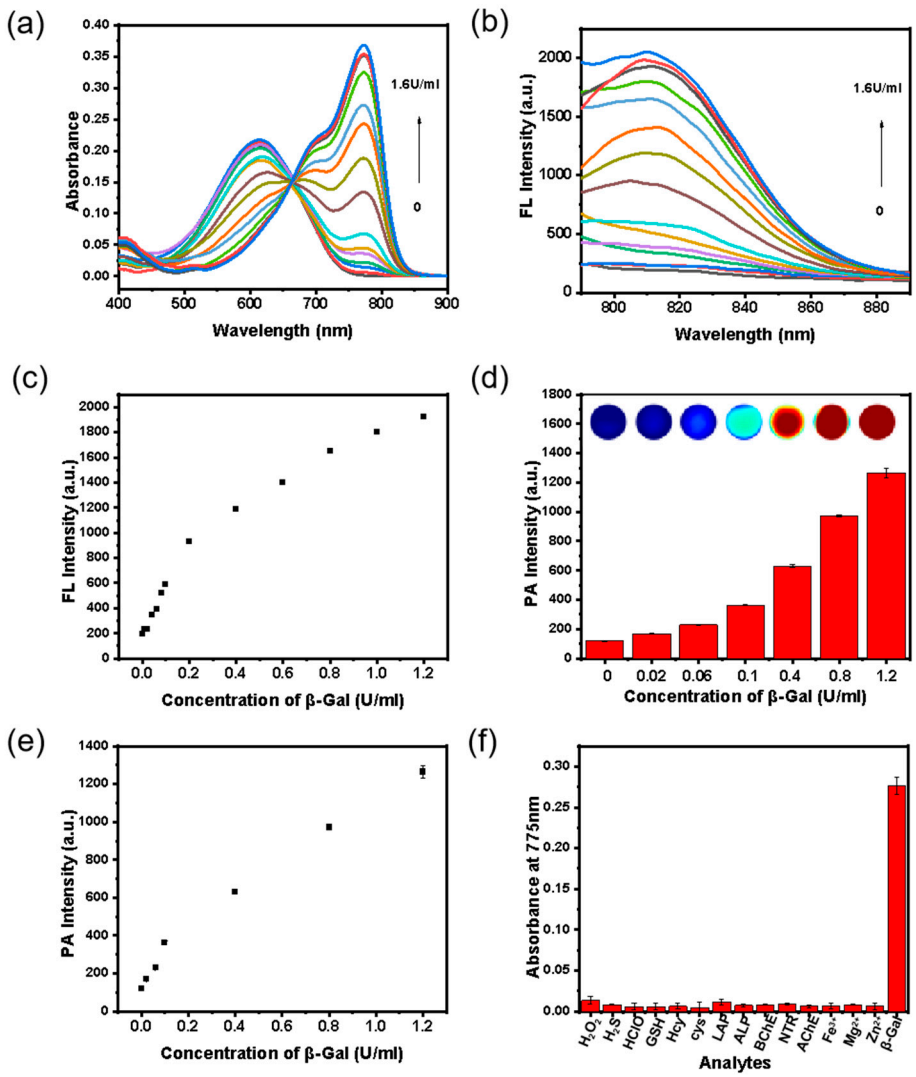

Figure 4. (**a**) Absorption and (**b**) fluorescence spectra of 5 μM Gal-QCS with 0–1.6 U/mL β-gal for 1 h. (**c**) Fluorescence intensity of 5 μM Gal-QCS to 0–1.2 U/mL β-gal in 810 nm. (**d**) Photoacoustic intensity of 5 μM Gal-QCS with 0–1.2 U/mL β-gal for 1 h. (**e**) Photoacoustic intensity of 5 μM Gal-QCS to 0–1.2 U/mL in 775 nm. (**f**) Absorbance of Gal-QCS at 775 nm in the presence of various analytes. (1) H_2O_2 (100 μM), (2) H_2S (100 μM), (3) HClO (100 μM), (4) GSH (1 mM), (5) Hcy (100 μM), (6) Cys (100 μM), (7) LAP (50 U/L), (8) ALP (50 U/L), (9) BChE (50 U/L), (10) NTR (50 U/L), (11) AChE (50 U/L), (12) Fe^{2+} (500 μM), (13) Mg^{2+} (500 μM), (14) Zn^{2+} (500 μM), (15) β-Gal (2 U/mL).

3.3. Fluorescence Imaging of Cells

Based on the detection results of β-gal by Gal-QCS in vitro, we applied Gal-QCS to β-gal imaging in living cells. Before conducting the cell imaging experiment, we used the MTT assay to detect the toxicity of Gal-QCS to evaluate its biocompatibility. As shown in Figure S10, after incubation with different concentrations of Gal-QCS for 24 h, the viability of Hela cells in all experimental groups was higher than 80%. In addition, after incubating Gal-QCS in 4T1 cells for 24 h, the cell viability also exceeded 80%, indicating that Gal-QCS has no obvious cytotoxicity in biological imaging applications and has good biocompatibility.

Due to the excellent performance of Gal-QCS in response speed, selectivity, and stability, it is used for the fluorescence imaging of β-gal in living cells. 4T1 are cells with positive expression of β-gal, while Hela are cells with negative expression of β-gal. Probe Gal-QCS (5 μM) was incubated with 4T1 cells and Hela cells at 37 °C for 1 h. As a result, the

fluorescence intensity in the red channel of 4T1 cells was significantly enhanced, whereas that of Hela cells was minimal. Moreover, the fluorescence intensity of 4T1 cells in the red channel was 7.59-fold that of Hela cells (Figure 5a,b). This result indicates that probe Gal-QCS can selectively image 4T1 tumor cells.

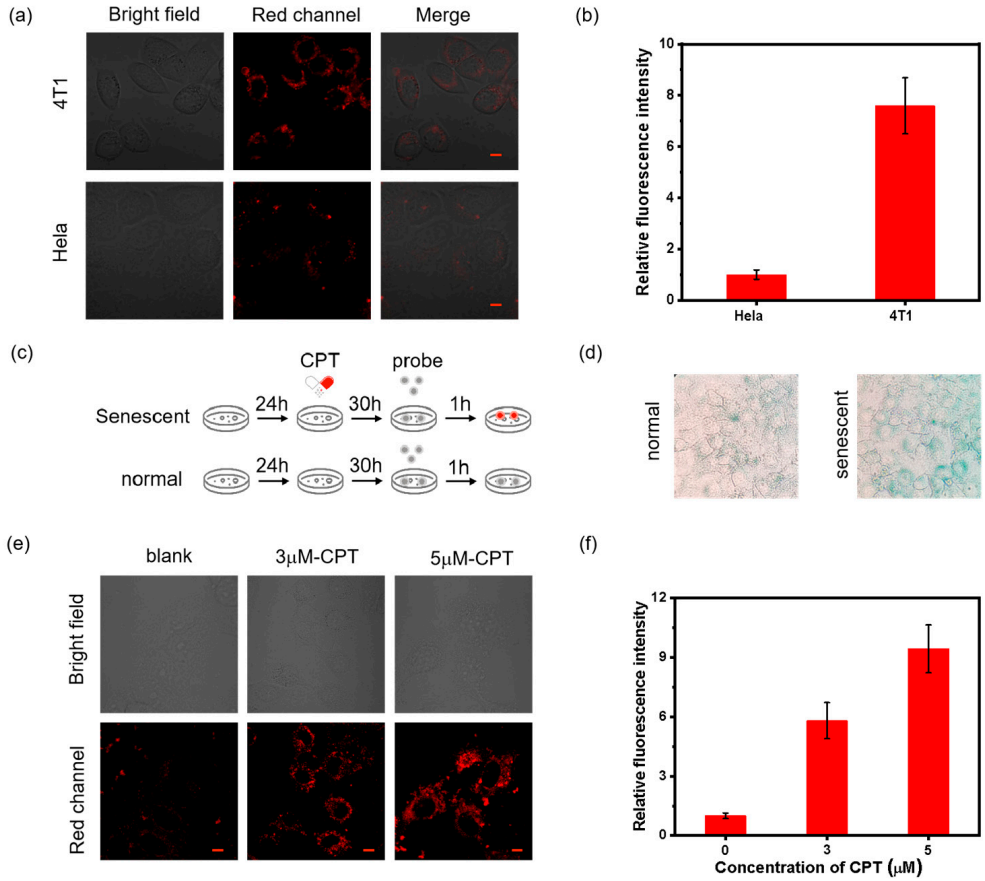

Figure 5. (**a**) Confocal images of Hela cells, 4T1 cells incubated with Gal-QCS (5 μM) for 1 h. (**b**) Relative fluorescence intensity of Hela cells and 4T1 cells from red channels. (**c**) Schematic diagram of cell drug administration. (**d**) CPT-induced senescent Hela cell images determined by X-gal kits. (**e**) Confocal images of CPT-induced senescent Hela cells with Gal-QCS (5 μM) for 1 h. (**f**) Relative fluorescence intensity of Hela cells from red channels. Ex/Em = 640/663–738 nm. Scale bars, 10 μm.

It is known that in addition to being overexpressed in 4T1 tumors, β-gal is also closely associated with the process of cellular senescence. Therefore, we selected senescent cells as the model to study β-gal activity. CPT is an anticancer drug that can induce the premature senescence of cells. Therefore, we established CPT-induced senescent HeLa cells as a representative senescence model and used Gal-QCS to detect endogenous β-gal in this cell model (Figure 5c). After treatment with different concentrations of CPT for 30 h, β-gal staining was performed with a commercial kit X-gal to evaluate premature senescence (Figure 5d). After incubation with Gal-QCS for 1 h, the fluorescence intensity in the red channel of senescent Hela cells was significantly enhanced, while normal HeLa cells had almost no fluorescence signal in the red channel. In normal Hela cells, the fluorescence in the red channel can be ignored, whereas obvious red fluorescence can be observed in senescent cells (Figure 5e). For senescent cells induced by adding 5 μM CPT, after probe addition, the red channel fluorescence was 9.43-fold that of normal cells (Figure 5f). The above results indicate that Gal-QCS selectively images β-gal in senescent cells and 4T1 cells.

3.4. In Vivo Tumor Imaging

β-gal is over-expressed in cancer cells such as those of ovarian cancer and breast cancer. The practical feasibility of Gal-QCS for real-time in vivo visualization of β-gal activity was evaluated in 4T1 tumor-bearing mice. To explore the ability of Gal-QCS to perform FL/PA bimodal imaging of β-gal in vivo, we selected the subcutaneous 4T1 tumor-bearing mouse model as the research object. The practical feasibility of Gal-QCS for real-time in vivo visualization of β-gal activity was evaluated in tumor-bearing mice. We injected Gal-QCS into the tumor of mice, and at the same time subcutaneously injected the same amount of Gal-QCS into the normal tissues of mice. As shown in Figure 6a, within 5 min, obvious NIR fluorescence and photoacoustic signals were specifically collected in the tumor area and gradually increased with time. At 30 min, the fluorescence intensity of the tumor area was 8.10-fold that of the initial value (Figure 6b), and at the same time, the photoacoustic signal at the tumor site was also enhanced by 1.97-fold (Figure 6c,d), while there was no obvious signal change in normal tissues, indicating that Gal-QCS can be quickly activated at the tumor site.

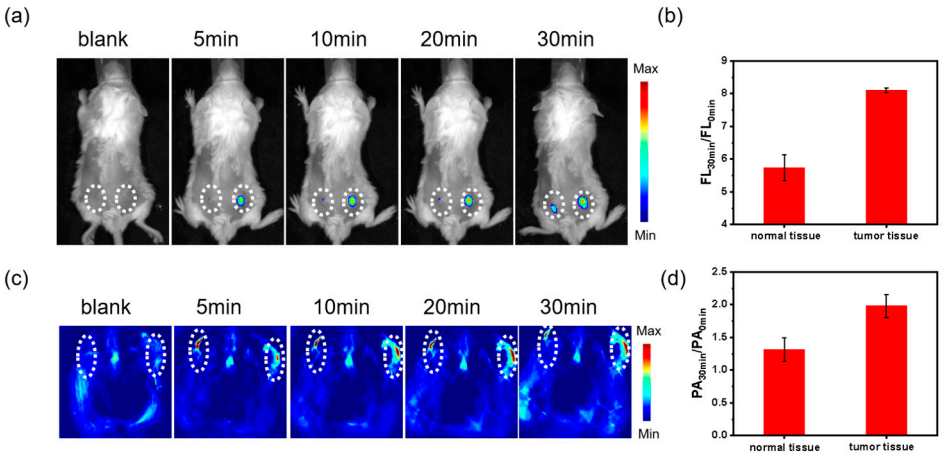

Figure 6. (**a**) Fluorescence images of 4T1 tumor-bearing mice after the injection of Gal-QCS for 5 to 30 min. Ex/Em = 710/820–880 nm. (**b**) 30 min after the subcutaneous injection of the probe, fluorescence intensity enhancement from the selected areas of mice. (**c**) Photoacoustic images of 4T1 tumor-bearing mice after the injection of Gal-QCS for 5 to 30 min. (**d**) 30 min after the subcutaneous injection of the probe, photoacoustic intensity enhancement from the selected areas of mice.

3.5. In Vivo Imaging of Drug-Induced Senescence

We performed imaging of liver senescence in mice using Gal-QCS. Balb/c mice were randomly divided into two groups, namely the CPT-induced senescence group and the normal PBS group. In the senescence group, liver senescence was induced in mice via gavage administration. The CPT (6 mg/kg) was given once every 2 days for 8 days. On the 10th day, mice in the senescence group were injected with Gal-QCS (100 μM, 100 μL) through the tail vein for imaging (Figure 7a). The successful construction of the senescence model can be verified by the liver sections (Figure S11). In the tissue sections of senescent liver, hepatocytes exhibit an increase in volume. The nuclear-cytoplasmic ratio decreases, and the cell nuclei undergo pyknosis, manifested as a reduction in nuclear volume, condensation of chromatin, and intense staining. Mice in the normal PBS group were also injected with Gal-QCS (100 μM, 100 μL) through the tail vein for imaging. Quantitative analysis shows that the fluorescence intensity of the liver in the senescence group was 10.53-fold that of the initial value, and that in the normal PBS group was 5.37-fold that of the initial value (Figure 7b,c). In addition, the photoacoustic signal of the liver in the CPT group shows a similar trend to the fluorescence signal. Specifically, the

photoacoustic intensity of the liver in the CPT group at 30 min was 1.43-fold that of the initial value, while that in the normal PBS group was only 1.02-fold that of the initial value (Figure 7d,e). These results confirm that Gal-QCS can effectively accumulate in the liver region in vivo and perform visual imaging of liver senescence.

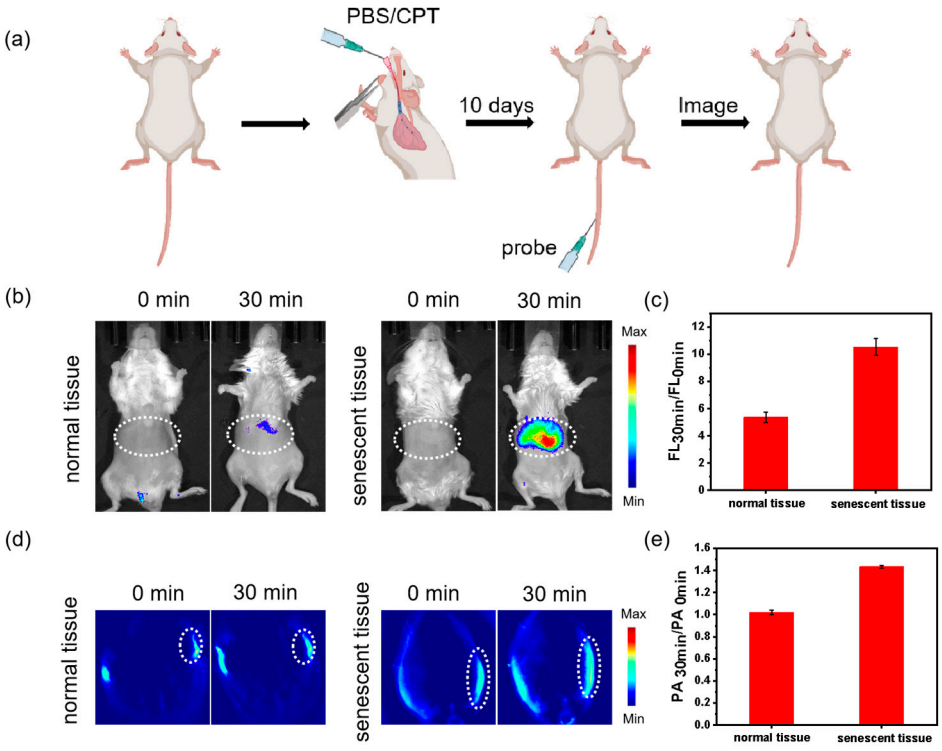

Figure 7. (**a**) Graphical description of the senescence experimental protocol and animal model construction. All mice were adaptively fed for 10 days. (**b**) Fluorescence images of normal mice and senescent mice after the injection of Gal-QCS for 0 to 30 min. Ex/Em = 710/820–880 nm. (**c**) 30 min after injection of the probe in the tail vein, fluorescence intensity enhancement from the selected areas of mice. (**d**) Photoacoustic images of normal mice and senescent mice after the injection of Gal-QCS for 0 to 30 min. (**e**) 30 min after injection of the probe in the tail vein, photoacoustic intensity enhancement from the selected areas of mice (The white dashed-line circle indicates the liver).

4. Discussion

In summary, in the forefront exploration of the field of biosensing and imaging, we have developed an innovative NIRF/PA bimodal probe, Gal-QCS. Its core application is focused on the precise detection of β-gal, a key biomarker. A fluorophore with a hemicyanine skeleton serves as the signal-reporting group, and a pyran galactoside group functions as a highly specific β-gal recognition unit. Through the precise molecular recognition mechanism between them, targeted binding to the target enzyme is achieved. In the NIR fluorescence mode, Gal-QCS exhibits remarkable sensitivity and can detect β-gal at extremely low concentration levels. In complex in vitro biochemical detection environments, in the face of various potential interfering factors, Gal-QCS not only maintains a stable detection performance but also has an ideal photoacoustic signal-to-noise ratio, providing a solid guarantee for the precise quantitative analysis of β-gal. Compared with numerous enzyme-responsive probes reported currently, Gal-QCS has significant advantages. It can achieve a rapid response within just 5 min, greatly shortening the detection time. Moreover, in complex biological matrices, it shows extremely high selectivity for β-gal, effectively avoiding detection errors caused by cross-reactions. In terms of biosafety assessment, the results of MTT cytotoxicity evaluation clearly indicate that Gal-QCS has good biocompatibility and can be safely and stably applied in in vivo animal experiments, laying a

solid foundation for subsequent pre-clinical research and translational applications. At the cellular level, Gal-QCS performs outstandingly in the field of live-cell imaging. It can monitor in real time and dynamically the overexpressed β-gal in 4T1 tumor cells, clearly presenting its distribution and activity changes in the tumor microenvironment. Meanwhile, for β-gal produced during the process of drug-induced cell senescence, it can also achieve high-resolution imaging, providing a powerful visualization tool for the study of the cell senescence mechanism. More notably, this probe can acutely capture the changes in the expression level and distribution of β-gal during the process of organ aging, enabling the early and precise detection of organ senescence. Therefore, Gal-QCS is of great significance for the early diagnosis of drug-induced organ senescence. It is expected to become a core tool in the field of organ aging detection, helping to intervene in advance and delay the organ aging process, opening up new ideas for the prevention and treatment of senescence-related diseases. Particularly crucially, the synthesis route of Gal-QCS is simple and efficient, and the raw material costs are low, which endows it with great potential for widespread application in large-scale scientific research experiments and pre-clinical studies.

Supplementary Materials: The following supporting information can be downloaded at: https://www.mdpi.com/article/10.3390/chemosensors13020074/s1, Scheme S1: Synthetic route for Gal-QCS; Table S1: Compounds used in the synthesis process; Figure S1: Absorption spectra of QCS and Bn-QCS (5 μM, 30% EtOH); Figure S2: Fluorescence spectral changes of Gal-QCS (5 μM) in the presence of β-gal (2 U/mL). Ex = 640 nm; Figure S3: Time-dependent photoacoustic response of Gal-QCS (5 μM, 30% EtOH) toward β-gal (2 U/mL). The collection wavelength is 775 nm; Figure S4: Mass spectrometry characterization of Bn-QCS by MALDI-TOF; Figure S5: Mass spectrometry characterization of Gal-QCS by MALDI-TOF; Figure S6: Characterize the response of probe Gal-QCS after adding β-gal by MALDI-TOF mass spectrometry; Figure S7: Linear fitting curve of the FL intensity of 5 μM Gal-QCS to 0–0.2 U/mL β-gal; Figure S8: Linear fitting curve of the PA intensity of 5 μM Gal-QCS to 0–0.1 U/mL β-gal; Figure S9: The response of probe Gal-QCS in different pH environments; Figure S10: Cell viability of 4T1 cells, Hela cells after co-incubation with Gal-QCS at various concentrations from 0 to 30 μM; Figure S11: Representative photomicrographs of H&E staining of liver sections from mice fed with different concentrations of camptothecin (0–6 mg/kg); Figure S12: 1HNMR spectra of compound Bn-QCS; Figure S13: 13CNMR spectra of compound Bn-QCS; Figure S14: 1H NMR spectra of compound Gal-QCS.

Author Contributions: Conceptualization: X.-B.Z., X.Y., Y.-H.Y., L.Y. and T.-B.R.; Methodology: Y.-H.Y., Software: Y.-H.Y., L.-L.R., P.-Z.L. and W.Z.; Validation: Y.-H.Y., L.-L.R. and W.Z.; Data curation: Y.-H.Y., P.-Z.L., W.Z., T.-B.R. and X.Y.; Writing—original draft preparation: Y.-H.Y. and J.-L.Z.; Writing—review and editing: X.-B.Z., X.Y., J.-L.Z., L.Y. and T.-B.R.; Supervision: X.-B.Z., X.Y., L.Y. and T.-B.R.; Project administration: X.Y.; Funding acquisition: X.Y. All authors have read and agreed to the published version of the manuscript.

Funding: This work was supported by the fund from the National Natural Science Foundation of China (Grants 21974039).

Institutional Review Board Statement: The animal study protocol was approved by the Laboratory Animal Center of Hunan and experiments were approved by the Animal Ethics Committee of College of Biology (Hunan University) (No. SYXK (Xiang) 2023-0010).

Informed Consent Statement: Not applicable.

Data Availability Statement: The original contributions presented in the study are included in the article/Supplementary Material, and further inquiries can be directed to the corresponding author.

Conflicts of Interest: The authors declare no conflicts of interest.

References

1. He, S.; Sharpless, N.E. Senescence in Health and Disease. *Cell* **2017**, *169*, 1000–1011. [CrossRef] [PubMed]
2. Kong, X.; Feng, D.; Wang, H.; Hong, F.; Bertola, A.; Wang, F.-S.; Gao, B. Interleukin-22 induces hepatic stellate cell senescence and restricts liver fibrosis in mice. *Hepatology* **2012**, *56*, 1150–1159. [CrossRef] [PubMed]
3. Marino, F.; Scalise, M.; Salerno, N.; Salerno, L.; Molinaro, C.; Cappetta, D.; Torella, M.; Greco, M.; Foti, D.; Sasso, F.C.; et al. Diabetes-Induced Cellular Senescence and Senescence-Associated Secretory Phenotype Impair Cardiac Regeneration and Function Independently of Age. *Diabetes* **2022**, *71*, 1081–1098. [CrossRef] [PubMed]
4. Muñoz-Espín, D.; Serrano, M. Cellular senescence: From physiology to pathology. *Nat. Rev. Mol. Cell Biol.* **2014**, *15*, 482–496. [CrossRef]
5. Blasco, M.A. Telomere length, stem cells and aging. *Nat. Chem. Biol.* **2007**, *3*, 640–649. [CrossRef]
6. Lee, H.W.; Heo, C.H.; Sen, D.; Byun, H.-O.; Kwak, I.H.; Yoon, G.; Kim, H.M. Ratiometric Two-Photon Fluorescent Probe for Quantitative Detection of β-Galactosidase Activity in Senescent Cells. *Anal. Chem.* **2014**, *86*, 10001–10005. [CrossRef]
7. Lozano-Torres, B.; Galiana, I.; Rovira, M.; Garrido, E.; Chaib, S.; Bernardos, A.; Muñoz-Espín, D.; Serrano, M.; Martínez-Máñez, R.; Sancenón, F. An OFF–ON Two-Photon Fluorescent Probe for Tracking Cell Senescence in Vivo. *J. Am. Chem. Soc.* **2017**, *139*, 8808–8811. [CrossRef]
8. Sun, B.; Luo, C.; Cui, W.; Sun, J.; He, Z. Chemotherapy agent-unsaturated fatty acid prodrugs and prodrug-nanoplatforms for cancer chemotherapy. *J. Control. Release* **2017**, *264*, 145–159. [CrossRef]
9. Minko, T.; Rodriguez-Rodriguez, L.; Pozharov, V. Nanotechnology approaches for personalized treatment of multidrug resistant cancers. *Adv. Drug Deliv. Rev.* **2013**, *65*, 1880–1895. [CrossRef]
10. Kakisaka, K.; Yoshida, Y.; Suzuki, Y.; Sato, T.; Kuroda, H.; Miyasaka, A.; Takikawa, Y. Serum markers for mitochondrial dysfunction and cell death are possible predictive indicators for drug-induced liver injury by direct acting antivirals. *Chem. Sci.* **2018**, *48*, 78–86. [CrossRef]
11. Gorgoulis, V.; Adams, P.D.; Alimonti, A.; Bennett, D.C.; Bischof, O.; Bishop, C.; Campisi, J.; Collado, M.; Evangelou, K.; Ferbeyre, G.; et al. Cellular Senescence: Defining a Path Forward. *Cell* **2019**, *179*, 813–827. [CrossRef] [PubMed]
12. Hernandez-Segura, A.; Nehme, J.; Demaria, M. Hallmarks of Cellular Senescence. *Trends Cell Biol.* **2018**, *28*, 436–453. [CrossRef] [PubMed]
13. Lian, Q.; Xu, J.; Yan, S.; Huang, M.; Ding, H.; Sun, X.; Bi, A.; Ding, J.; Sun, B.; Geng, M. Chemotherapy-induced intestinal inflammatory responses are mediated by exosome secretion of double-strand DNA via AIM2 inflammasome activation. *Cell Res.* **2017**, *27*, 784–800. [CrossRef] [PubMed]
14. Childs, B.G.; Baker, D.J.; Kirkland, J.L.; Campisi, J.; van Deursen, J.M. Senescence and apoptosis: Dueling or complementary cell fates? *EMBO Rep.* **2014**, *15*, 1139–1153. [CrossRef] [PubMed]
15. Schwarze, S.R.; Shi, Y.; Fu, V.X.; Watson, P.A.; Jarrard, D.F. Role of cyclin-dependent kinase inhibitors in the growth arrest at senescence in human prostate epithelial and uroepithelial cells. *Oncogene* **2001**, *20*, 8184–8192. [CrossRef]
16. Lee, B.Y.; Han, J.A.; Im, J.S.; Morrone, A.; Johung, K.; Goodwin, E.C.; Kleijer, W.J.; DiMaio, D.; Hwang, E.S. Senescence-associated β-galactosidase is lysosomal β-galactosidase. *Dev. Dyn.* **2006**, *5*, 187–195. [CrossRef]
17. de Mera-Rodríguez, J.A.; Álvarez-Hernán, G.; Gañán, Y.; Martín-Partido, G.; Rodríguez-León, J.; Francisco-Morcillo, J. Is Senescence-Associated β-Galactosidase a Reliable in vivo Marker of Cellular Senescence During Embryonic Development? *Front. Cell Dev. Biol.* **2021**, *9*, 623175. [CrossRef]
18. Collado, M.; Serrano, M. The power and the promise of oncogene-induced senescence markers. *Nat. Rev. Cancer* **2006**, *6*, 472–476. [CrossRef]
19. Zhang, J.; Cheng, P.; Pu, K. Recent Advances of Molecular Optical Probes in Imaging of β-Galactosidase. *Bioconjug. Chem.* **2019**, *30*, 2089–2101. [CrossRef]
20. Gao, Y.; Hu, Y.; Liu, Q.; Li, X.; Li, X.; Kim, C.-Y.; James, T.D.; Li, J.; Chen, X.; Guo, Y. Two-Dimensional Design Strategy to Construct Smart Fluorescent Probes for the Precise Tracking of Senescence. *Angew. Chem. Int. Ed.* **2021**, *60*, 10756–10765. [CrossRef]
21. Li, J.; Wang, L.; Luo, X.; Xia, Y.; Xie, Y.; Liu, Y.; Tan, W. Dual-Parameter Recognition-Directed Design of the Activatable Fluorescence Probe for Precise Imaging of Cellular Senescence. *Anal. Chem.* **2023**, *95*, 3996–4004. [CrossRef] [PubMed]
22. Li, X.; Qiu, W.; Li, J.; Chen, X.; Hu, Y.; Gao, Y.; Shi, D.; Li, X.; Lin, H.; Hu, Z.; et al. First-generation species-selective chemical probes for fluorescence imaging of human senescence-associated β-galactosidase. *Chem. Sci.* **2020**, *11*, 7292–7301. [CrossRef] [PubMed]
23. Chen, Z.; Mu, X.; Han, Z.; Yang, S.; Zhang, C.; Guo, Z.; Bai, Y.; He, W. An Optical/Photoacoustic Dual-Modality Probe: Ratiometric in/ex Vivo Imaging for Stimulated H_2S Upregulation in Mice. *J. Am. Chem. Soc.* **2019**, *141*, 17973–17977. [CrossRef] [PubMed]
24. St. Lorenz, A.; Buabeng, E.R.; Taratula, O.; Taratula, O.; Henary, M. Near-Infrared Heptamethine Cyanine Dyes for Nanoparticle-Based Photoacoustic Imaging and Photothermal Therapy. *J. Med. Chem.* **2021**, *64*, 8798–8805. [CrossRef]
25. Ma, G.; Gao, X.; Jiang, C.; Xing, S.; Wei, C.; Huang, P.; Lin, J. pH-Responsive Nanoprobe for In Vivo Photoacoustic Imaging of Gastric Acid. *Anal. Chem.* **2019**, *91*, 13570–13575. [CrossRef]

26. Fathi, P.; Knox, H.J.; Sar, D.; Tripathi, I.; Ostadhossein, F.; Misra, S.K.; Esch, M.B.; Chan, J.; Pan, D. Biodegradable Biliverdin Nanoparticles for Efficient Photoacoustic Imaging. *ACS Nano* **2019**, *13*, 7690–7704. [CrossRef]
27. Wang, L.V.; Hu, S. Photoacoustic Tomography: In Vivo Imaging from Organelles to Organs. *Science* **2012**, *335*, 1458–1462. [CrossRef]
28. Fan, X.-P.; Huang, J.; Ren, T.-B.; Yuan, L.; Zhang, X.-B. De Novo Design of Activatable Photoacoustic/Fluorescent Probes for Imaging Acute Lung Injury In Vivo. *Anal. Chem.* **2023**, *95*, 1566–1573. [CrossRef]
29. Yuan, M.; Fang, X.; Wu, Y.; Xu, Y.; Feng, H.; Mu, J.; Chen, Z.; Lin, Y.; Fu, Q.; Du, W.; et al. Activatable Nanoprobe with Aggregation-Induced Dual Fluorescence and Photoacoustic Signal Enhancement for Tumor Precision Imaging and Radiotherapy. *Anal. Chem.* **2022**, *94*, 5204–5211. [CrossRef]
30. Qu, J.; Teng, D.; Sui, G.; Guan, S.; Wang, Y.; Wang, Q.; Lin, Y.; Ran, H.; Wang, Z.; Wang, H. A photothermal-hypoxia sequentially activatable phase-change nanoagent for mitochondria-targeting tumor synergistic therapy. *Biomater. Sci.* **2020**, *8*, 3116–3129. [CrossRef]
31. Wu, F.Z.; Liu, J.J.; Tao, M.L.; Wang, M.; Ren, X.; Hai, Z. β-Galactosidase-Activatable Fluorescent and Photoacoustic Imaging of Tumor Senescence. *Anal. Chem.* **2023**, *95*, 10481–10485. [CrossRef] [PubMed]
32. Qin, Z.; Ren, T.-B.; Zhou, H.; Zhang, X.; He, L.; Li, Z.; Zhang, X.-B.; Yuan, L. NIRII-HDs: A Versatile Platform for Developing Activatable NIR-II Fluorogenic Probes for Reliable In Vivo Analyte Sensing. *Angew. Chem. Int. Ed.* **2022**, *61*, e202201541. [CrossRef] [PubMed]
33. He, L.; He, L.H.; Lai, H.; Xu, S.; Wang, J.; Xu, J.; Shi, L.; Yuan, L. Synergistic phototherapy of NIR wavelength xanthene-quinoline salt-based heavy-atom-free photosensitizers for tumor therapy. *Chem. Commun.* **2023**, *59*, 10745–10748. [CrossRef] [PubMed]
34. Liu, H.; Lv, R.; Song, F.; Yang, Y.; Zhang, F.; Xin, L.; Zhang, P.; Zhang, Q.; Ding, C. A near-IR ratiometric fluorescent probe for the precise tracking of senescence: A multidimensional sensing assay of biomarkers in cell senescence pathways. *Chem. Sci.* **2024**, *15*, 5681–5693. [CrossRef] [PubMed]